Noname manuscript No.
(will be inserted by the editor)

Impact of Local Terrain Features on Urban Airflow

Matthew Coburn · Christina Vanderwel · Steven Herring · Zheng-Tong Xie

Received: DD Month YEAR / Accepted: DD Month YEAR

Abstract Past work has shown that coupling can exist between atmospheric air flows at street scale (O(0.1 km)) and city scale (O(10 km)). It is generally impractical at present to develop high-fidelity urban simulations capable of capturing such effects. This limitation imposes a need to develop better parameterisations for meso-scale models but an information gap exists in that past work has generally focused on simplified urban geometries and assumed the buildings to be on flat ground. This study aimed to begin to address this gap in a systematic way by using the large eddy simulation method with synthetic turbulence inflow boundary conditions to simulate atmospheric air flows over the University of Southampton campus. Both flat and realistic terrains were simulated, including significant local terrain features, such as two valleys with a width about 50 m and a depth about average building height, and a step change of urban roughness height. The numerical data were processed to obtain averaged vertical profiles of time-averaged velocities and second order turbulence statistics. The flat terrain simulation was validated against high resolution particle image velocimetry data, and the impact of uncertainty in defining the turbulence intensity in the synthetic inflow method was assessed. The ratio between realistic and flat terrains of time-mean streamwise velocity

M. R. Coburn
Aerodynamics and Flight Mechanics, University of Southampton
E-mail: mc6g16@soton.ac.uk

Christina Vanderwel
Aerodynamics and Flight Mechanics, University of Southampton
E-mail: c.m.vanderwel@soton.ac.uk

Steven J. Herring
Aerodynamics and Flight Mechanics, University of Southampton
E-mail: s.herring@soton.ac.uk

Zheng-Tong Xie
Aerodynamics and Flight Mechanics, University of Southampton
E-mail: Z.Xie@soton.ac.uk

at the same ground level height over a terrain crest location can be greater than 2, while over a valley trough it can be less than 0.5. Further data analysis conclusively showed that the realistic terrain can have a considerable effect on global quantities, such as the depth of the spanwise-averaged internal boundary layer and spatially-averaged turbulent kinetic energy (TKE). These highlight the potential impact that local terrain features (O(0.1 km)) may have on near-field dispersion and the urban micro-climate.

Keywords Above-Ground-Level Height · Downslope · Street-scale Terrain · Water Tunnel Experiment · Velocity Modulation

1 Introduction

At present operational meso-scale models are unable to predict the details of urban flows at street and neighbourhood scale (i.e O(1 km)). Although finely resolved urban simulations can be generated by engineering computational fluid dynamics (CFD) codes (e.g. Xie and Castro, 2009; Han et al., 2017; Antoniou et al., 2017; Inagaki et al., 2017; Tolias et al., 2018; Gronemeier et al., 2020) over scales from 1 m to neighbourhood scale, larger city-scale simulations (i.e O(10 km)) are generally impractical. This presents a significant limitation, as past work has shown that two-way coupling can exist between the urban boundary layer properties measured at street scale (O(0.1 km)), neighborhood (O(1 km)), and city scales (O(10 km)) (Fernando, 2010; Barlow et al., 2017). Such coupling can be particularly pronounced when the urban area includes features such as a single or cluster of tall buildings (Han et al., 2017; Fuka et al., 2018; Hertwig et al., 2019), or a sharp change in topography (Conan et al., 2016; Blocken et al., 2015; Limbrey et al., 2016).

The development of simulations which accurately capture the coupling between street and city scales challenges both numerical and experimental approaches in many respects. This study uses numerical simulations to examine a selected heterogeneous area containing urban geometry and small sharp changes in topography (O(0.1 km)) in a systematic way which is difficult to achieve through wind and water tunnel experiments, or field observations.

Xie and Castro (2009) shows that to resolve the flow at street scale a grid resolution of a metre or less is necessary, but using such a resolution for city scale simulations challenges both current computational tools and resources. This imposes challenges because of the limited computational resources, and consequently the limited resolution. The complex geometries of real buildings must be simplified without losing any features which have a critical effect on the flow. Small topographic features (O(0. 1km)) impose similar challenges, which are typically smoothed and simplified in numerical and physical models. The first question is what are the critical - but perhaps small - features of buildings and terrain that must be resolved. The second question is whether special treatments are required.

Atmospheric flows around arrays of buildings with complex geometries have been investigated in a number of studies published since 2000, for example

Arnold et al. (2004); Xie and Castro (2009); Hertwig et al. (2012); Han et al. (2017); Antoniou et al. (2017); Inagaki et al. (2017); Tolias et al. (2018); Hertwig et al. (2019); Gronemeier et al. (2020); Sessa et al. (2020); Goulart et al. (2019); Ricci et al. (2020); Liu et al. (2023). These studies have principally addressed the challenges arising from heterogeneity and anthropogenic drivers as identified in Barlow et al. (2017), such as may be associated with step-changes in urban roughness height and development of internal urban boundary layer, a cluster of tall buildings and local thermal stratification. As such, they have generally assumed the buildings to be on flat ground and neglected the effect of terrain.

A few studies that have considered the effects of urban terrain have focused on city-scale (O(10 km)) topographic changes (e.g. Fernando, 2010). This may be because they have aimed to support meso-scale model developers striving to increase their spatial resolution (e.g. to O(1 km)) and capture the average effects of small topographic features without resolving them. A small number of papers (Apsley and Castro, 1997; Blocken et al., 2015; Conan et al., 2016) have studied the airflow over small scale terrain without any buildings, and emphasized the crucial role of small terrain features. An exception is the work of Fossum and Helgeland (2020) which included ambitious large-eddy simulations (LES) for the hilly city of Oslo using a domain of 150 km^2 at a spatial resolution of 2 m. The work aimed to demonstrate the capability of LES to provide detailed data for developing parameterisations for a fast-response tool. They emphasized the importance of the wall boundary conditions in particular, which is linked to the importance of small-scale topographic features.

At present there is uncertainty in the role of small-scale topography on the street and neighbourhood scale which, through coupling, can result in uncertainty on the city scale. This highlights a need for new studies to investigate and understand the effects of small-scale topographic features on street (O(0.1 km)) to neighborhood (O(1 km)) scales, before considering the coupling between neighborhood and city scales.

2 The Case Study of Southampton University Highfield Campus

The city of Southampton lies at the confluence of the Test and Itchen rivers and the urban area contains numerous small valleys. Two such valleys are shown by the dark areas in Fig. 1 and the dark blue in Fig. 2, cross the University of Southampton Highfield campus. In Fig. 2 the positive x and y coordinates are west-east and south-north respectively. To the west of the campus is a 1 km (west-east) by 2 km (south-north) public park, in which the terrain is flat with a small downslope of approximately 1:50 from north to south. With these features in westerly wind, the campus is an excellent site for conducting a study to examine the importance of small (O(0.1 km)) and sharp changes in terrain elevation within a real urban area. Due to the complications involved in taking account of tree effects into the LES, trees in the park and in the campus were ignored entirely. The current case study is a considerably simplified one for terrain effect.

The approach adopted for assessing the significance of small scale topography was to compare the simulations of atmospheric air flows around the buildings in the campus for cases in which the buildings were on flat and on real terrain (including the small-scale topography). To validate the numerical modelling method for neutral atmospheric conditions, advantage was taken of the availability of high resolution PIV data from a water tunnel experiment.

The domain chosen for the study was sized to include sufficient surrounding area to capture the flow development over the buildings upstream of the campus and the downstream evolution of the wakes created by the campus buildings. This led to a final domain which comprised the Highfield campus plus the surrounding area out to 80 m, which was equivalent to $5h$, where h was the average building height of 16 m within the study domain. The packing density was 29%. In Fig. 2a and b the solid black line at y=104 m indicates the streamwise-vertical $(x - z)$ plane in which the PIV data were taken, while the solid black line at $y = -210$ m indicates an example $x - z$ plane for further data analysis (e.g. see Fig. 4d).

Figure 2a shows the domain for the flat terrain case which has dimensions 900 m (L_x^F) × 800 m (L_y^F). Figure 2b shows the domain of the real terrain case, with dimensions 1050 m (L_x^T) × 800 m (L_y^F). The domain for the real terrain case includes a 150 m extension upstream of $x = 0$, to allow the spanwise variation in terrain elevation at the location $(x = 0, y)$ to be linearly interpolated to zero terrain elevation at the corresponding inlet location ($x = -150$ m, y), creating a rectangular shape inlet plane required by the synthetic turbulence inflow (STI) conditions. This treatment is similar as that for wind tunnel experiments. The first valley which has a width of about 50 m and a depth of about 10 m is between x =200 m − 400 m (Fig. 2b). The second deeper and narrower valley between $x = 800$ m − 900 m is near the outlet of the CFD domain and was not the focus of this study.

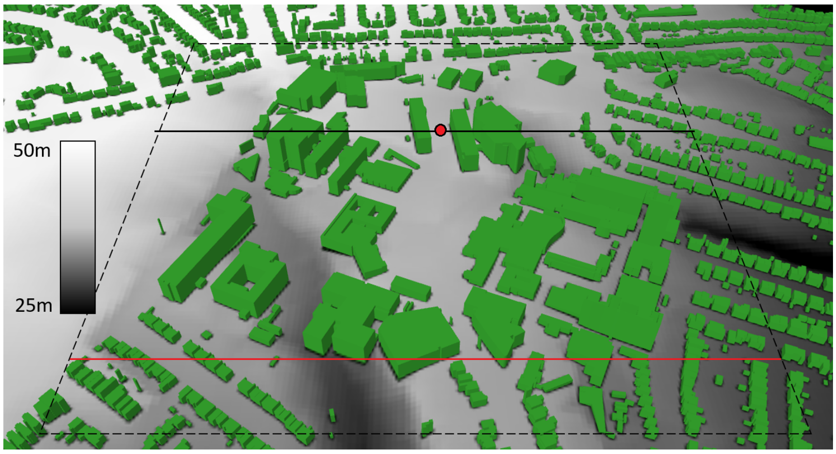

Fig. 1: Three-dimensional geometry and terrain contours (above sea-level) of the University of Southampton Highfield campus. The dashed frame shows the extent of computational domain. The red dot marks Location 7 (Fig. 5). The black solid line indicates the streamwise-vertical $(x-z)$ plane in which the PIV data were taken, while the red solid line indicates the streamwise-vertical $(x-z)$ plane shown in Fig. 4d

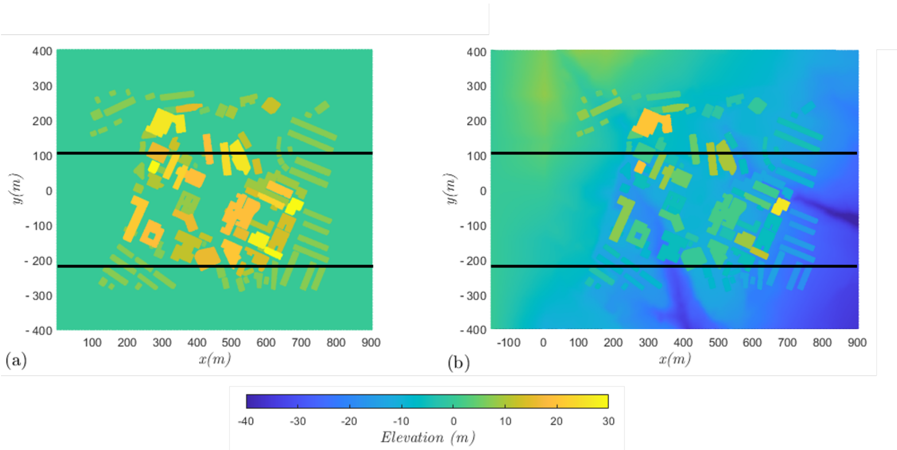

Fig. 2: Contours of the terrain and building elevation for a) the flat terrain cases (SF8,FF8, SF12) with the ground placed at elevation $z = 0$, and b) real terrain case (ST8 ext.) with the inlet ground located at elevation $z = 0$. The black solid line at $y = 104$ m indicates the streamwise-vertical $(x - z)$ plane in which the PIV data were taken, while the black solid line at $y = -210$ m indicates an example $x - z$ plane for further analysis (i.e. Fig. 4d)

2.1 Setting Details of Study Cases

The LES case geometries for the study were developed using building footprint and height data from the OS MasterMap data set and Ordnance Survey (OS) 5 m resolution terrain data. The simulation cases created are summarised in Table 1. For consistency with the physical model placed on the flat floor in the water-tunnel (flume) experiment, all the buildings were modelled as having flat roofs. The errors resulting from this simplification should be small as the university campus buildings generally have flat roofs, and the replacing the pitched roofs with flat ones on the small number of residential houses in the surrounding area should not produce large errors. The building heights of the water tunnel model and the cases SF8, SF12, FF8 were defined based on the longest vertical edges of the flat-roof buildings from the OS MasterMap data set, which avoids any ambiguity due to the terrain, and the average building height was denoted h.

The mesh generator SnappyHexMesh in OpenFoam v2.1.1 was used to create conformal (body-fitted) meshes (Coburn et al., 2022). The flat terrain case in which the real terrain was replaced with flat terrain and a grid developed with a resolution of 2m ($h/8$) was denoted SF8 (Table 1). The ratio of the domain height and the average building height h of SF8 was 12, which was close to the ratio of the water tunnel boundary layer thickness and the average building height h. To verify that the grid was sufficient, a case denotes SF12 with a finer resolution of $h/12$ was also simulated. The case FF8 had the same other settings as SF8, except for its inflow mean velocity and Reynolds stresses obtained from the naturally grown turbulent boundary layer in the water-tunnel experiments (Fig. 3c and d), for the purpose of a direct comparison with the PIV data (see Table 1). The physical model had a Reynolds number $Re_h \approx 3{,}080$ (Sect. 3.2), based on the average building height and the freestream velocity. The Reynolds number based on the average building height and freestream velocity for cases SF8, SF12 and FF8 was 16,000, while it was 13,600 for SF8 ext. and ST8 ext. Early studies (e.g. Stoesser et al., 2003; Cheng and Castro, 2002; Xie and Castro, 2006; Xie et al., 2008) suggested that Reynolds number dependency (if it does exists) was very weak for such flows. For example, the Reynolds number based on the bulk velocity and the cube height in a study of flow over an array of cubes mounted on a channel wall was 3,823 (Stoesser et al., 2003), while it was 4,790 based on the average height and freestream velocity in a study of an array of random height blocks (Xie et al., 2008).

To avoid any blockage issue for the simulations of real terrain, the domain height was increased to $15h$ (denoted ST8 ext. in Table 1). More interestingly, if building height is defined as the height difference between the roof and the average ground level around the perimeter of the building, adding the real terrain leads to 15% reduction in average building height compared to the water tunnel model. To have a closer comparison between flat terrain and real terrain, a new flat terrain case SF8 ext. (Table 1) was built with a domain height $15h$ and an average building height 13.6m in full scale, equivalent to

15% reduction in average building height, compared to the water tunnel model and the cases SF8, FF8.

Given that the primary aim of the study was to examine the flow in a real urban area, synthetic turbulence inflow boundary (STI) conditions (e.g. Xie and Castro, 2008) were used throughout as it can replicate turbulent inflow conditions better than using periodic boundary conditions. However, as the inflow turbulence quantities may be subject to considerable uncertainty as they are difficult to obtain from observations, theoretical estimation, or down-scaling from meso-scale models, a sensitivity test was carried out with respect to the inflow turbulence levels.

The inflow conditions applied to cases SF8 and SF12 were taken from (Xie and Castro, 2009) and are shown in Fig. 3a and b. The conditions used were originally derived from wind tunnel experiments conducted in the EnFlo wind tunnel at the University of Surrey as part of the DAPPLE project, in which a thick turbulent boundary layer was generated using the so-called "simulated atmospheric boundary layer" approach (Counihan, 1969). This involved placing several large vortex generators at the wind tunnel inlet, and evenly distributed numerous small roughness elements on the floor between the inlet and the array of buildings. The roughness length $z_0 = 0.0018m$ was equivalent to 0.0018 boundary thickness in Xie and Castro (2009), and equivalent to $0.02h$ in Fig. 3a. For this study the STI vertical Reynolds stress profiles were scaled so that the peak Reynolds stress occurred approximately at the average building height. Below the peak height the Reynolds stress data were estimated through linear interpolation. "DAPPLE" in the "STI Input" column in Table 1 denotes the EnFlo wind tunnel data, while "FLUME" denotes the water tunnel data described in Sect. 3.2. The inflow mean streamwise velocity and Reynolds stresses at $0 \leq z/h \leq 12$ for cases SF8 ext. and ST8 ext. were respectively the same as in Figs. 3 a and b, while the data at $12 < z/h \leq 15$ were constants respectively equal to those at $z/h = 12$.

Symmetry boundary condition was applied for the top and the two lateral boundaries, constant pressure was applied for the outlet, no-slip wall boundary condition was applied for ground and building surfaces. It usually took about 60 wall-clock hours on 200 cores to complete one simulation case with the initialisation period $80T_p$, and the averaging period $130T_p$, where T_p was the characteristic time based on the average building height and the free stream velocity.

Cases	**Resolu.**	**Domain size/h (x,y,z)**	**STI Input**
Flat terrain (**SF8**)	$h/8$	56.25, 50, 12	DAPPLE
Flat terrain(**SF12**)	$h/12$	56.25, 50, 12	DAPPLE
Flume flat terrain(**FF8**)	$h/8$	56.25, 50, 12	FLUME
Flat terrain & Taller domain(**SF8 ext.**)*	$h/8$	56.25, 50, 15	DAPPLE
Real terrain & taller domain(**ST8 ext.**)*	$h/8$	65.625, 50, 15	DAPPLE

Table 1: Summary of the Highfield Campus simulation cases. The resolution is that within the canopy. *Cases SF8 ext. and ST8 ext. have an average building height $0.85h$.

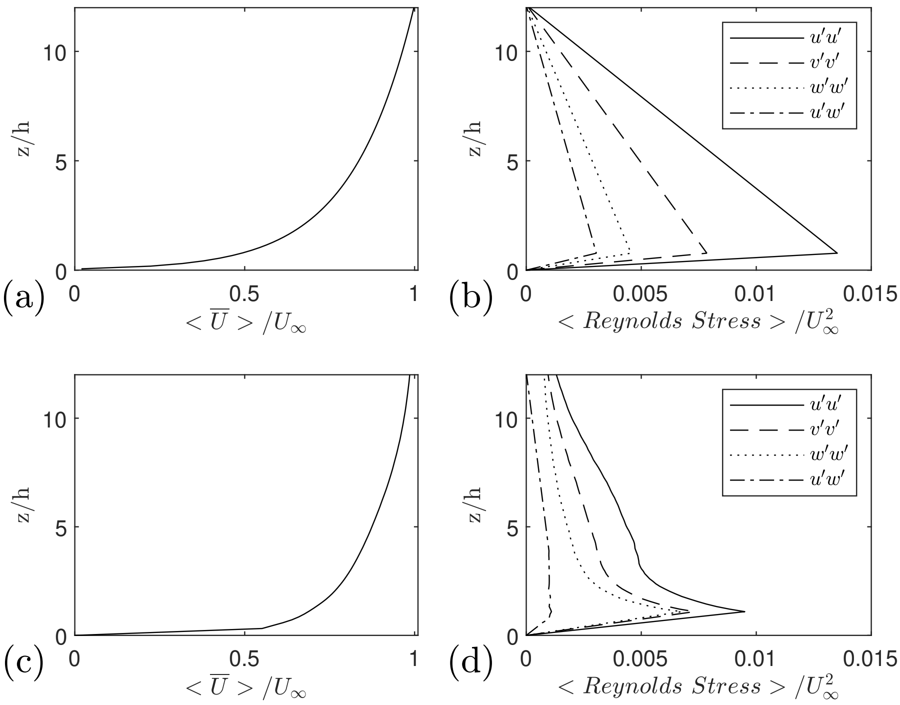

Fig. 3: Flow conditions of the experiments just upstream of the building cluster. a) mean streamwise velocity and b) Reynolds stresses from the EnFlo wind tunnel data (Xie and Castro, 2009). c) mean streamwise velocity and d) Reynolds stress from the flume experiments (see Sect. 3.2)

2.2 Terrain Elevation Analysis

Figure 2 plots the contours of terrain and building elevation with the inlet ground located at $z = 0$ for the flat terrain cases SF8, SF12 and FF8 (Fig.

2a) and the real terrain case ST8 ext. (Fig. 2b). Case ST8 ext. has a gentle downward slope across the streamwise extent (west-east) of the domain, and a gentle downward slope across the north-south extent of the domain. An estimation of the "average slope" in west-east direction would be helpful to understand flow field in the western wind.

The ground elevation was defined as $E(x, y)$. The building elevation was ignored, while a linear interpolation was applied between the upstream and downstream building edges to fill in the gaps left by removing the building. The average ground elevation $AE(y)$ over the entire streamwise extent at y was calculated by averaging $E(x, y)$ over the x range. The average gradient of the slice at y was defined as the ratio of $AE(y)$ to the half length of the domain in the streamwise direction. Figure 4 shows $x - z$ slices at the spanwise locations $y = -28$ m, -102 m, -181 m and -210 m, respectively. The vertical line in each sub-figure marks the location where the valley crosses the $x - z$ plane. The spanwise-averaged slope gradient of the terrain elevation is approximately $-2.3°$.

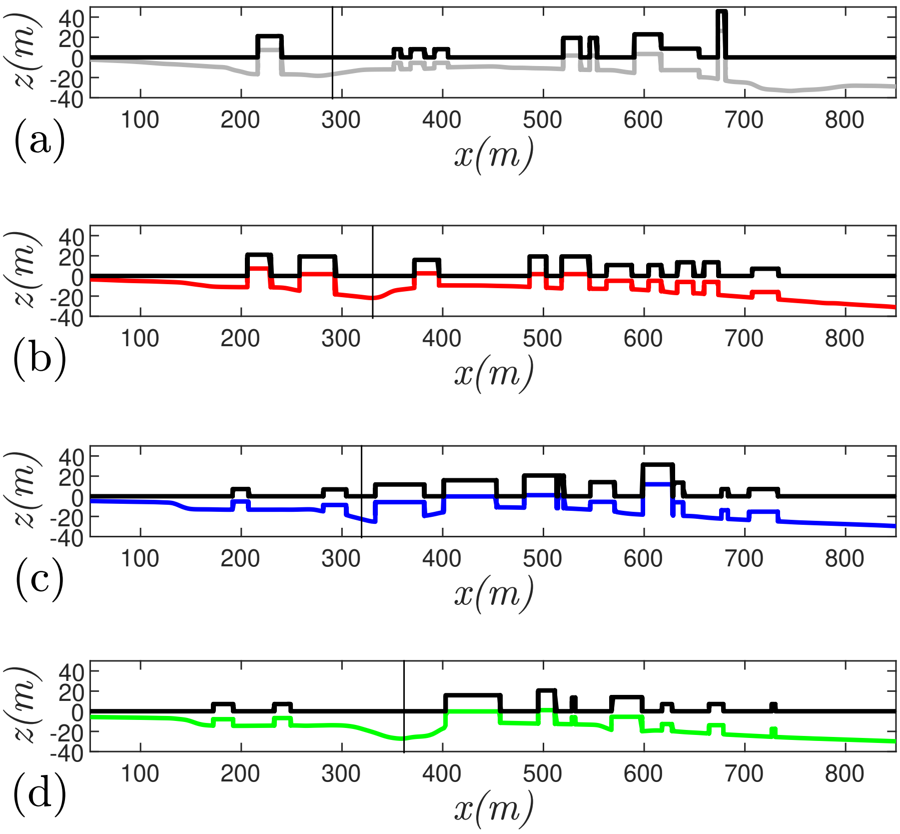

Fig. 4: Streamwise terrain and building profiles at four different spanwise locations, a) $y = -28$ m, b) $y = -102$ m, c) $y = -181$ m and d) $y = -210$ m (see Fig. 2 for the y coordinate). Thick black lines denote the flat terrain and buildings. Thick coloured lines denote the real terrain and buildings. Vertical black line in a) denotes Station 1 at $(x, y) = (292$ m, -28 m$)$. Vertical black line in b) denotes Station 2 at $(x, y) = (336$ m, -102 m$)$. Vertical black line in c) denotes Station 3 at $(x, y) = (332$ m, -152 m$)$. Vertical black line in d) denotes Station 4 at $(x, y) = (376$ m, -210 m$)$

For statistics of the distribution of terrain and building elevation for each $x - z$ slice shown in Fig. 4, the average linear slope for the slice was subtracted from the elevation. The statistical data, i.e. mean, r.m.s., skewness and kurtosis, are given in Table 2. The elevation data for the flat terrain case SF8 ext. in Table 2 are consistently more skewed than those for the real terrain case ST8 ext. This is because the flat terrain contributes many zero elevation points to the data-set. The addition of real terrain (ST8 ext.) leads to more Gaussian distributions in elevation.

Case	Slice Location **y** (m)	Mean Height (m)	r.m.s.	Skewness	Kurtosis
SF8 ext.	-28	5.009	8.4107	1.705	5.890
ST8 ext.	-28	7.128	11.196	1.689	6.571
SF8 ext.	-102	4.480	6.045	0.824	2.054
ST8 ext.	-102	8.276	8.284	0.243	2.000
SF8 ext.	-180	5.039	6.812	1.166	3.634
ST8 ext.	-180	9.505	9.607	0.937	3.949
SF8 ext.	-210	2.866	4.732	1.309	3.551
ST8 ext.	-210	7.008	8.035	0.306	2.483
SF8 ext.	Domain Av.	3.478	5.200	1.000	3.026
ST8 ext.	Domain Av.	6.384	7.424	0.635	3.001

Table 2: Terrain and building elevation statistics in four $x-z$ planes ($y = -28$ m, -102 m, -180 m and -210 m) for cases SF8 ext. and ST8 ext.

3 Numerical Method and PIV data

3.1 Large Eddy Simulation Method

The study was based on using the LES method to capture the inherent unsteadiness of the atmospheric air flows which develop in urban areas (e.g. Kanda et al., 2004; Xie and Castro, 2006; Castro et al., 2017; Wingstedt et al., 2017). Equations 1 and 2 show the grid-size averaged (filtered) continuity and Navier-Stokes equations respectively,

$$\frac{\partial u_i}{\partial x_i} = 0, \tag{1}$$

$$\frac{\partial u_i}{\partial t} + \frac{\partial u_i u_j}{\partial x_j} = -\frac{1}{\rho}\frac{\partial p}{\partial x_i} + \nu \frac{\partial^2 u_i}{\partial x_j \partial x_j} - \frac{\partial \tau_{ij}}{\rho \partial x_j}, \tag{2}$$

where u_i and p are the resolved or filtered velocity and pressure respectively, τ_{ij} is the Subgrid-scale Reynolds stress, ρ is the air density, and ν is the kinematic viscosity, x_i denotes the coordinates, and t denotes time. The mixed time scale sub-grid scale (SGS) model (Inagaki et al., 2005) was used to avoid using the near wall damping functions required in the Smagorinsky SGS model. However, reports in the literature (e.g. Xie and Castro, 2009) suggest that because the flow is largely building block-scale dependent the airflow should be relatively insensitive to the precise nature of the SGS model, as long as the grid resolves the inertial range of the turbulence spectra. The LES model embedded in the open-source package OpenFOAM v2.1.1 was used. A second-order backward implicit scheme in time and second-order central difference scheme in space were applied for the discretization in the finite volume method approach. More details of methodology can be found in Sessa et al. (2020); Coburn et al. (2022).

3.2 Particle Image Velocimetry Data

An important part of the study was to validate a simulation of the atmospheric airflow around the Highfield Campus buildings on flat terrain with experimental data. The data used was high resolution particle image velocimetry (PIV) data obtained from experiments conducted in the University of Southampton's 6.75 m long re-circulating water tunnel (see more details in Lim et al. (2022)) using a 1:2400 scale 3D printed model. It should be noted that the water tunnel model was a simplification in that all the building roofs were made flat, whether they actually were or not. The freestream velocity of the water tunnel experiments was $U_\infty = 0.46$ ms^{-1}. The average building height was $h = 6.7$ mm at model scale. This leads to a Reynolds number of $Re_h \approx 3080$ based on the average building height and the freestream velocity. The model was exposed to a naturally developed boundary layer (Fig. 3c and d). The boundary layer thickness was 83 mm, resulting in a boundary layer thickness to average building height ratio of approximately 12.

The particle image velocimetry (PIV) measurements of the velocity fields were obtained using two 4 mega pixel CMOS cameras and a 100mJ Nd:YAG double pulsed laser. A total of 2000 image pairs were captured at a separation time of 1200 μs and sampling rate of 2 Hz. LaVision's DaVis 8.4.0 software was used for post-processing of the particle images to produce vector maps. The uncertainty in the velocity was estimated to be 2%, mostly due to image distortion and refraction affecting the magnification factor at the edges of the images.

The PIV data used in the study was taken in the streamwise vertical plane equivalent to $y = 104$ m (full scale) in the computational domain (see Figure 2). Vertical profiles were extracted at 14 locations given IDs 1–14 counting from upstream to downstream, starting from a position equivalent to $x =$ 220 m (13.3h) and then at 40 m intervals ($\Delta x = 2.5h$).

4 Urban Airflow Over the flat Terrain

4.1 Validation against PIV measurements

Figures 5 and 6 show comparisons between the PIV data obtained in the naturally grown turbulent boundary layer and data from the LES case FF8. In both figures the squares are the PIV data showing every fifth data point, while the solid line is the LES data. Vertical profiles of mean streamwise and vertical velocities (Fig. 5), and u_{rms}, w_{rms} and $\overline{u'w'}$ (Fig. 6) at the 14 stations defined in Section 3.2 starting at $x = 13.3h$ with an interval $\Delta x = 2.5h$ are shown. Figure 5 shows slight under-predictions in the LES data at some locations. The discrepancy in the mean axial velocity is within 5% of the experimental data. The vertical velocity differs slightly more, but agreement between the mean velocity profiles in Fig. 5 appears as good as might be expected when comparing to PIV data from a small scale model.

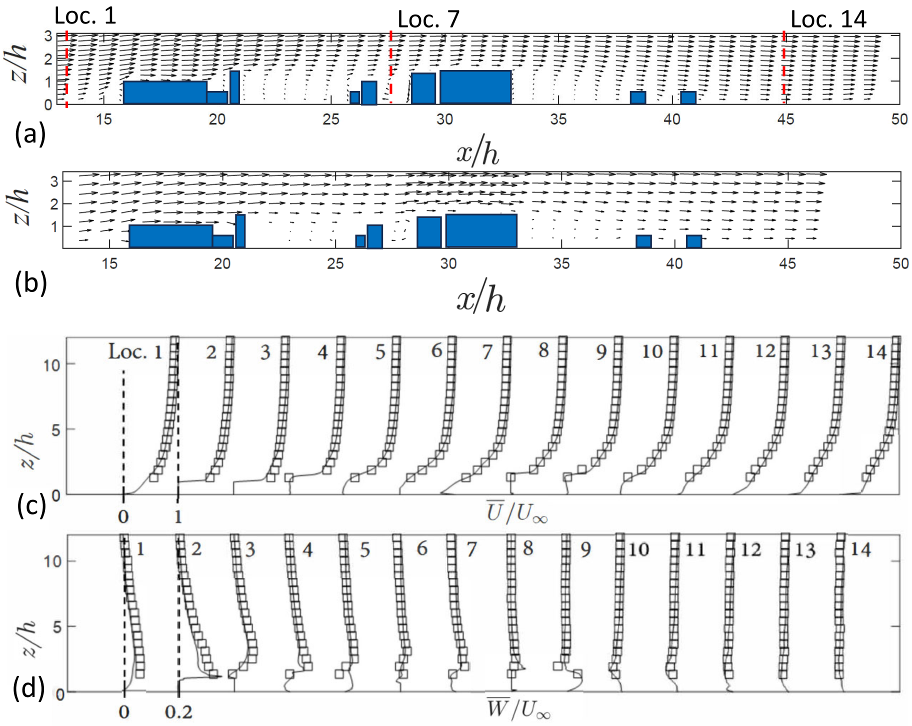

Fig. 5: a) LES case FF8 and b) PIV velocity vectors in vertical plane at y =104 m. c) mean normalised streamwise velocity. d) mean normalised vertical velocity. lines, LES data; squares, PIV data

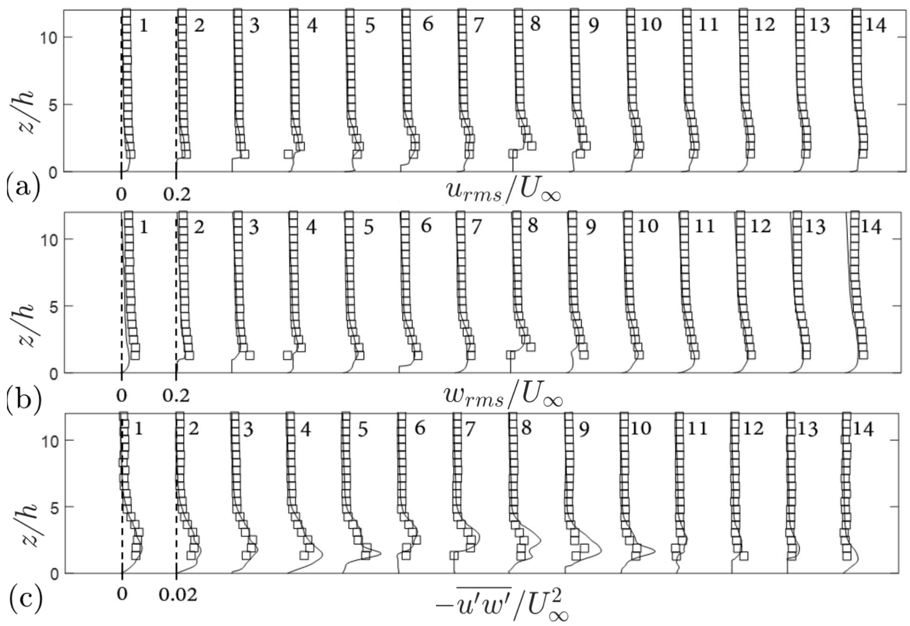

Fig. 6: a) Normalised r.m.s. streamwise velocity fluctuations b) normalised r.m.s. vertical velocity fluctuations, and c) normalised mean Reynolds shear stress. lines, LES data; squares, PIV data

Figure 6 shows profiles of the r.m.s. streamwise and vertical velocity fluctuations and the mean Reynolds shear stress. There is a small under-prediction of the peak values which occur close to the ground and building surfaces, for example in the fourth profile in Fig. 6, but also an over-prediction of the mean Reynolds shear stress at locations 8-10, again close to building surfaces. Discrepancies of this type were expected in the near-wall region, as the quality of the PIV data was affected by high intensity reflections from the model surface. The agreement is very good in the regions devoid of reflections from the laser sheet and dominated by the free shear layers which develop downstream of the roughness elements. Overall, the level of agreement between the PIV data and the case FF8 with the inflow conditions based on the water tunnel turbulence quantities is very promising.

4.2 Effects of Inflow Turbulence Quantities

Two sets of turbulent inflow quantities were used (see Fig. 3). The integral length scales used for all cases in this study were the same as those as in Xie and Castro (2009), which were $4h$ in the streamwise direction, and $1h$ in the vertical and lateral (spanwise) directions. The effect of different inflow turbulence quantities was evaluated by looking at Location 7 (Fig. 5) which was approximately $15h$ downstream of the leading edge of building array, placed in a narrow canyon between two highest (1.5h) buildings in the $y = 104$ m plane (Fig. 2). Figures 7 and 8 show comparisons of mean velocities and turbulence statistics at Location 7 for two sets of inflow conditions and two grid resolutions.

Figure 7 generally shows only very small differences in the mean velocities predicted in cases FF8 and SF8, suggesting that the effect of the inflow turbulence quantities on mean flow is small. This confirmed the findings in other published studies (e.g. Macdonald et al., 2000; Hanna et al., 2002; Xie and Castro, 2008; Sessa et al., 2020; Fossum and Helgeland, 2020). Macdonald et al. (2000); Hanna et al. (2002) which reported that the mean flow and the turbulence fields typically approached equilibrium values after three rows of obstacles, which occurred at about $8h$ downstream, while Xie and Castro (2008); Sessa et al. (2020) reported that after more than 6 rows (approximately $12h$ downstream) the flow and turbulence fields can be considered being in equilibrium state, and Location 7 was at $15h$.

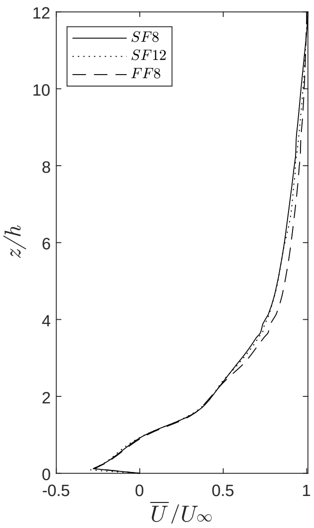

Fig. 7: Vertical profiles of mean normalised streamwise velocity at Location 7 (Fig. 5)

Figure 8 shows that the differences in the second order moments of turbulence statistics between cases SF8 and FF8 are small within and immediately above the canopy (e.g. below $z = 1.5h$), but increase above $z = 1.5h$, which is the height of the building upstream of Location 7. The differences increase substantially at heights above $z = 4h$ where the effect of the urban canopy diminishes and the large difference in turbulence level between the two inflow conditions becomes apparent (Fig. 3). This is because the inlet Reynolds stresses for the case FF8 are substantially less than for the other two cases. The smaller differences below $z = 1.5h$ are consistent with the findings in Xie and Castro (2008) that the turbulence statistics predicted by LES within and immediately above canopy relatively insensitive to the inflow turbulence quantities, so long as they are not too unrealistic, and the distance between the inlet and the sampling location is large enough (e.g. greater than $14h$).

Considering the sensitivity to grid resolution, Figures 7 and 8 show smaller differences in the data from cases SF8 and SF12, than between cases SF8 and FF8. Overall, it was concluded that the resolution and inflow conditions used in case ST8 ext. provided reliable data, and that data from SF8 could be used for the assessing the effect of terrain.

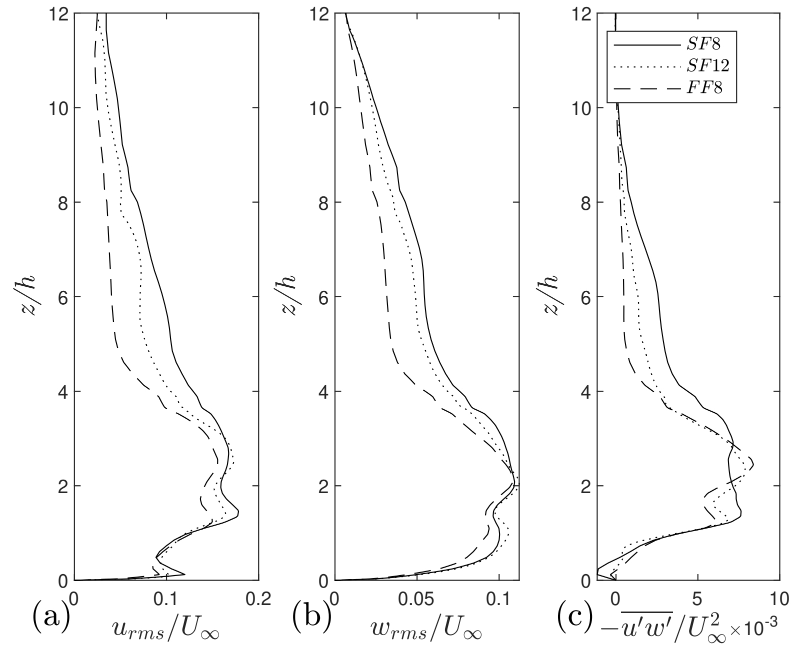

Fig. 8: Same as in Fig. 7, but for a) normalised streamwise velocity fluctuation r.m.s., b) normalised vertical velocity fluctuation r.m.s. and c) normalised vertical Reynolds shear stress

5 Local Terrain Effects – a Comparison between Flat (SF8 ext.) and Realistic (ST8 ext.) Terrains

5.1 Spatially Averaged Quantities

Spatially averaging fluid quantities over a domain that captures real topological features is not trivial. The method adopted in this study is to average data at the same above ground level (AGL) height as defined in Equation 3:

$$\langle\phi\rangle_f(z_{AGL}) = \frac{1}{S_t}\int_{(S_f)} \phi(x, y, z_{AGL})dxdy, \tag{3}$$

where ϕ denotes the quantity to be spatially-averaged, $\langle\rangle_f$ denotes the spatial average over the area not covered by buildings, which is approximately 71% of the ground surface within the study domain. S_f denotes the total area not covered by buildings and is constant over the entire AGL height z_{AGL}. In other words, it does not take into account the fluid region that is above a building, and of which the coordinates (x, y) are within the ground perimeter of the buildings. This ensures that inconsistencies are not introduced when using Eq. 3.

To identify the impact of the variation of terrain elevation, hereafter only data from cases SF8 ext. and ST8 ext. were the focus for comparison. All quantities were normalised by the spatially-averaged mean streamwise velocity U_{6h} at $z = 6h$. The spatially-averaged mean velocities and turbulence statistics are shown in Fig. 9. Albeit the large local differences in the ratio of mean velocities (e.g. Fig.12 b and c), Figures 9a shows a negligible difference in the spatially averaged dimensionless streamwise velocity between the flat (SF8 ext.) and real (ST8 ext.) terrain cases. By linearly extrapolating the Reynolds shear stress (Fig. 9c) to estimate the effectively friction velocity $u_*/U_{6h} = 0.096$, a best fitting of the $< U >$ data above $z_{AGL} = 4h$ to a logarithmic profile gave $z_0 = 0.08h$, and displacement $d = 0.5h$, which were not dissimilar to those in Castro et al. (2017).

Below $z_{AGL} = 2h$, the dimensionless Reynolds shear stress are essentially the same for the two cases SF8 ext. and ST8 ext., while the dimensionless turbulent kinetic energy for the case ST8 ext. is slightly less. Above $z_{AGL} = 2h$, the case ST8 ext. shows slightly greater turbulent kinetic energy and Reynolds shear stress, which is likely due to the local terrain elevation variation. The flat terrain case SF8 in Fig. 9 shows a visible difference in the streamwise velocity, turbulent kinetic energy and Reynolds shear stress, compared to the flat terrain case SF8 ext. This was due to the 15% greater average building height, and the 25% less domain height in the case SF8. The overall difference is not significant.

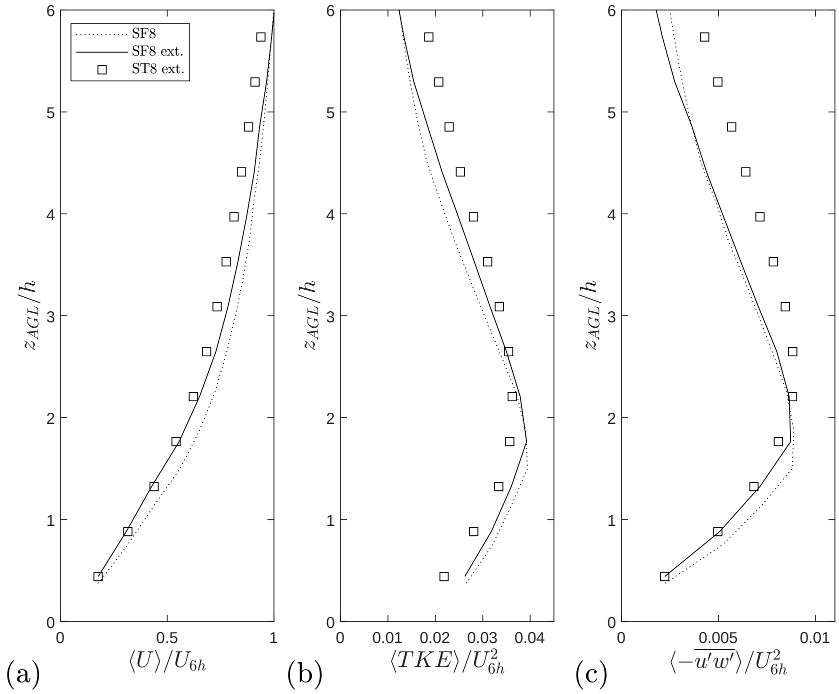

Fig. 9: Dimensionless spatially-averaged a) mean-streamwise velocity, b) turbulent kinetic energy and c) Reynolds shear stress, for cases SF8, SF8 ext. and ST8 ext.

5.2 Flow and Turbulence at Typical Locations

Figure 10 shows the mean streamwise velocity and Reynolds shear stress profiles at the same 14 locations in the plane y =104 m as in Fig. 5. The turbulence statistics on the vertical profiles are set to zero below the ground and building surfaces. Figure 10 reveals a visible difference in the mean streamwise velocity from including terrain, but the effect on vertical Reynolds shear stress is much greater. It was noted that at some locations the vertical mean velocity was sensitive to where the data was sampled (not shown). This suggests that given such sensitivities it might be extremely difficult to get close agreement in vertical mean velocity when comparing numerical and small scale physical simulations.

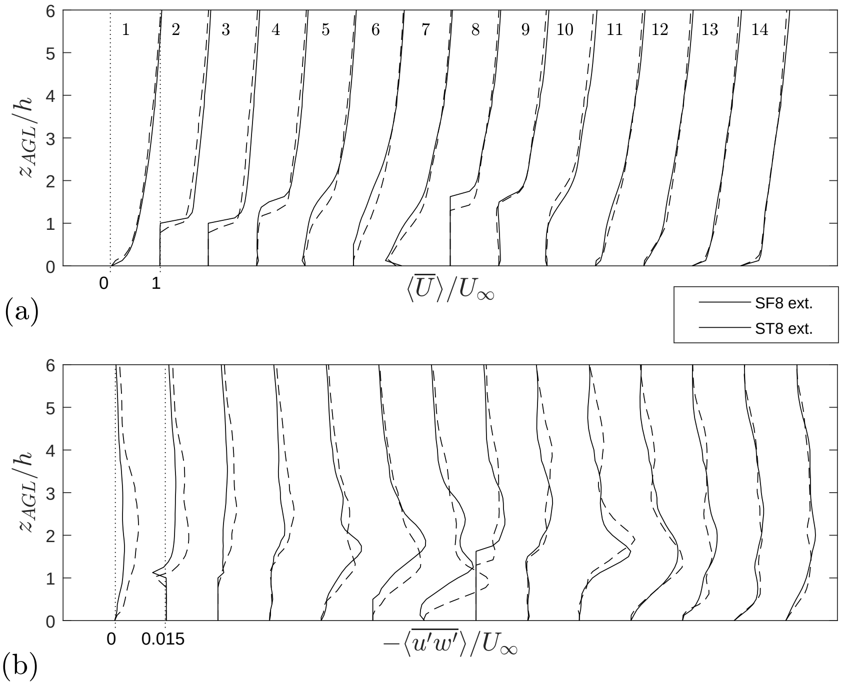

Fig. 10: Vertical profiles across an (x, z_{AGL}) plane at $y = 104$ m for a) mean streamwise velocity, and b) vertical Reynolds shear stress at the 14 stations shown in Fig.5. z_{AGL} is the local above ground height. U_{6h} is the spatially-averaged mean streamwise velocity at $z_{AGL} = 6h$. For building locations, see Fig.5a

Figure 11 shows a comparison of mean streamwise velocities in the (x, z) plane at $y = -210$ m shown in Fig. 2, for the flat (SF8 ext.) and real (ST8 ext.) terrain cases. Figure 11a shows that the boundary layer depth remains almost constant throughout the flat terrain domain. This suggests that the inflow boundary conditions were set appropriately to produce a fully developed flow across the domain. Figure 11b, however, shows that the boundary layer depth increases more evidently as it develops downstream, which is due to the terrain variation.

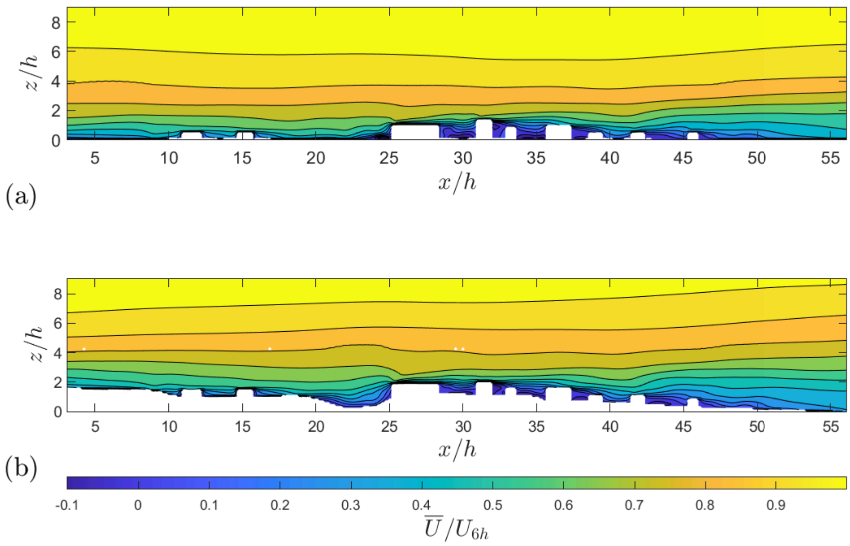

Fig. 11: Mean streamwise velocity in the (x, z) plane at $y = -210$ m shown in Fig.2 for a) SF8 ext. and b) ST8 ext.

To quantify the effect of terrain on the local mean velocity, the ratio of mean streamwise velocity is defined,

$$\overline{U}_{ST8}/\overline{U}_{SF8} = \frac{\|\overline{U}_T(x, y, z_{AGL})\|}{\|\overline{U}_F(x, y, z_{AGL})\|}, \tag{4}$$

where $\|\overline{U}_T(x, y, z_{AGL})\|$ and $\|\overline{U}_F(x, y, z_{AGL})\|$ are the absolute values of the mean streamwise velocity for the real terrain case ST8 ext., and the flat terrain case SF8 ext., respectively.

Figure 12a shows the elevation contours of the real terrain in the valley region ($0 \leq x/h \leq 40$, $-15 \leq y/h \leq 0$). Fig. 12 b and c show the ratio $\overline{U}_{ST8}/\overline{U}_{SF8}$ of the mean-streamwise velocities at $z_{AGL}/h = 0.56$ and 2.3, respectively. It is to be noted the fluid regions above buildings are not shown. The ratio $\overline{U}_{ST8}/\overline{U}_{SF8}$ correlated positively well with the terrain elevation. In general, a high elevation location was associated with a high ratio $\overline{U}_{ST8}/\overline{U}_{SF8}$, and vice versa. At an AGL height of more than twice average building height (i.e. $2.3h$), within and immediate downwind of the valley that was approximately $5h$ in width and h in depth, the ratio $\overline{U}_{ST8}/\overline{U}_{SF8}$ showed a minimum less than 70% above the valley, and a maximum 120% immediately downwind of the valley. Within the urban canopy at an AGL height of $0.56h$, the correlation between the mean streamwise velocity ratio and the terrain elevation was even more evident, albeit the disturbance due to the buildings. Th correlation between the terrain elevation and streamwise velocity was because the boundary layer flow could not immediately adjust to “body-fit” the local terrain, in particular at the valley trough and the crest. The enhanced streamwise velocity at the valley crest could also be due to the so-called “Bernoulli effect”. The visual strength of the correlation between elevation and mean streamwise velocity ratio suggests that it might be used to account for local terrain effects when flat terrain has to be used in experiments or numerical simulations.

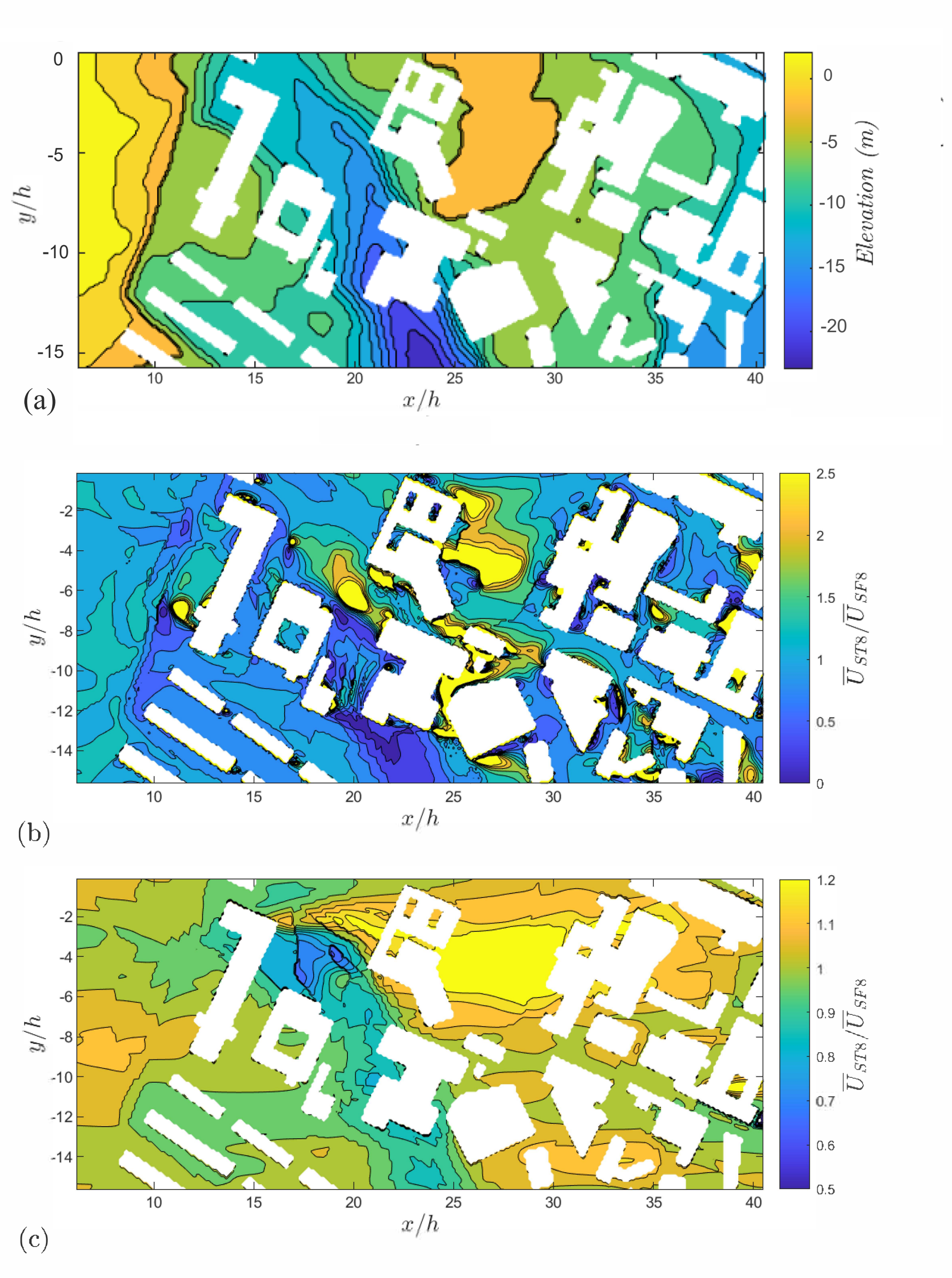

Fig. 12: a) Elevation contours of the real terrain in ST8 ext. with the inlet ground placed at elevation $z = 0$ as in Fig. 2, b) the ratio $\overline{U}_{ST8}/\overline{U}_{SF8}$ of the mean-streamwise velocity for ST8 ext. and SF8 ext. at $z_{AGL}/h = 0.56$, and c) at $z_{AGL}/h = 2.3$. The fluid regions above the buildings are not shown but left blank

Figure 13 shows contour plots of the dimensionless turbulent kinetic energy at $z_{AGL}/h = 0.56$ for cases SF8 ext. and ST8 ext. For most of the area, the TKE within the canopy for the real terrain case was lower than that in the flat terrain one (see Fig. 9). Figure 13a shows high TKE in front and behind large buildings. This was because 1) higher TKE at the average building height (see Fig. 3) was entrained into this altitude, and 2) the large buildings produced more turbulence into the wake region. Compared to the flat terrain case, Figure 13b shows less evident increase in TKE in front and behind large buildings, in particular over the valley region. Low TKE was expected over the valley region at $z_{AGL} = 0.56h$ as the deep valley preventing convection of high TKE into low altitude. Another reason was perhaps due to the downslope, which effectively reduced the average altitude of buildings.

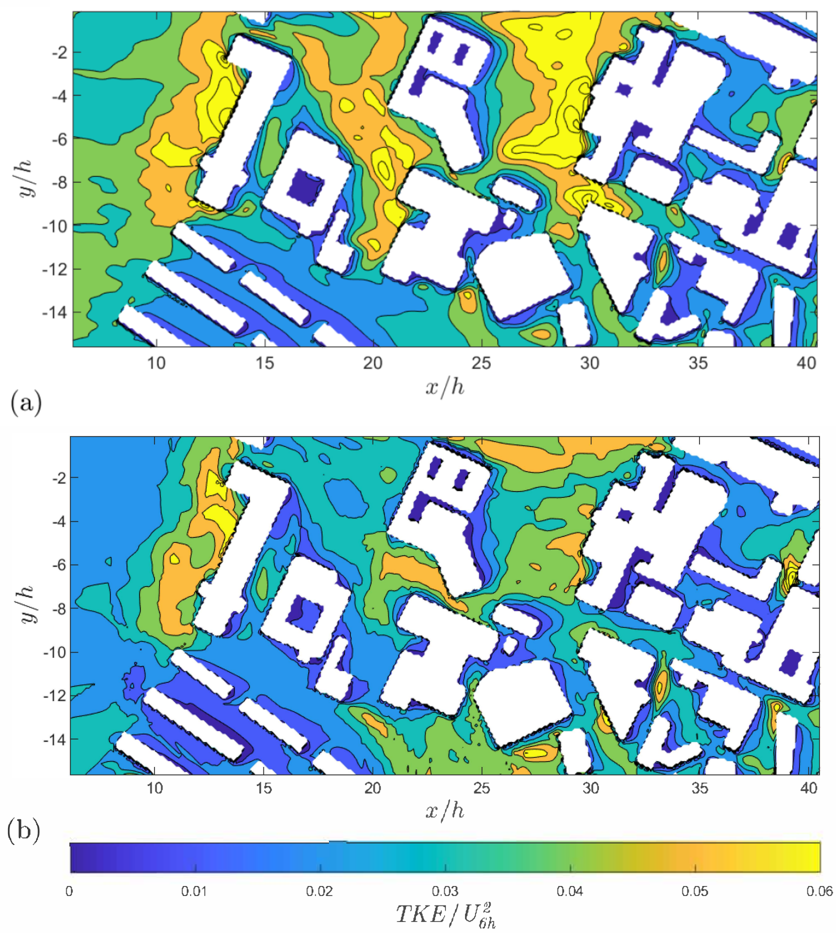

Fig. 13: Dimensionless turbulent kinetic energy at $z_{AGL} = 9$ m ($0.56h$) for a) SF8 ext., and b) ST8 ext.

Due to the difference in local packing density, the size of the buildings, the spatial scale and the amplitude of the terrain elevation variation, the effect of terrain on the local flow and turbulence quantities differed substantially from place to place. In this study we focused on four typical stations located in the valley (see Fig. 4). Figure 14a shows vertical profiles of mean streamwise velocity at the four stations for the flat (SF8 ext.) and real (ST8 ext.) terrains. At station 4 the valley was deep and wide and had a significant effect on mean streamwise velocity. At station 3, the effect of the valley was also evident. At stations 1 and 2, the effect of terrain on the mean streamwise velocity was much less. This was because the valley was very shallow at stations 1 and 2, and tall buildings were immediately upstream of them which played a more dominant role on the local wind.

Figure 14b-d show normal stresses $\overline{u'u'}$, $\overline{w'w'}$ and Reynolds shear stress $\overline{u'w'}$, respectively. These second order turbulence statistics were highly dependent on the local terrain and upstream buildings. Approximately 60m upstream of station 1, a tall and wide L shape building was located, from where a steep velocity gradient (Fig. 14a) and a strong shear layer with great turbulent kinetic energy and Reynolds shear stress at the building height (Fig. 14b-d) were generated and convected downstream. A square shape building was placed 30m upstream of station 2, which had an above-ground level height approximately 20 m, produced an evident shear layer (Fig. 14a) and increased turbulent kinetic energy and Reynolds stress (Fig. 14b-d) at the building height at station 2. Overall, the tall buildings upstream of stations 1 and 2 played a dominant role on the local wind field and turbulence, and the downstream valley enhanced this effect.

Station 3 was located in a narrow spacing between buildings in the valley, where the vertical profiles of $\overline{U}/U_{6h}$, $\overline{u'u'}/U_{6h}$ and $\overline{u'w'}/U_{6h}$ were respectively similar to those at station 2, but with a weaker shear layer at the local building height. The $\overline{w'w'}/U_{6h}$ in the vicinity of the ground was very different between the flat and real terrains, which was because of the narrow spacing between buildings and the steep terrain gradient. There were no large and tall buildings immediately upstream of station 4. The vertical profiles of mean streamwise velocity, Reynolds normal and shear stresses for case SF8 ext. hardly showed an evident shear layer at the average building height h, whereas those for case ST8 ext. showed a weak local shear layer at $0.5h$, which was caused by the gentle slope approximately 70 m upstream. This means that it would be extremely challenging to develop a simple method to precisely account for the effect of terrain and so correct the turbulent stresses obtained from a flat terrain model.

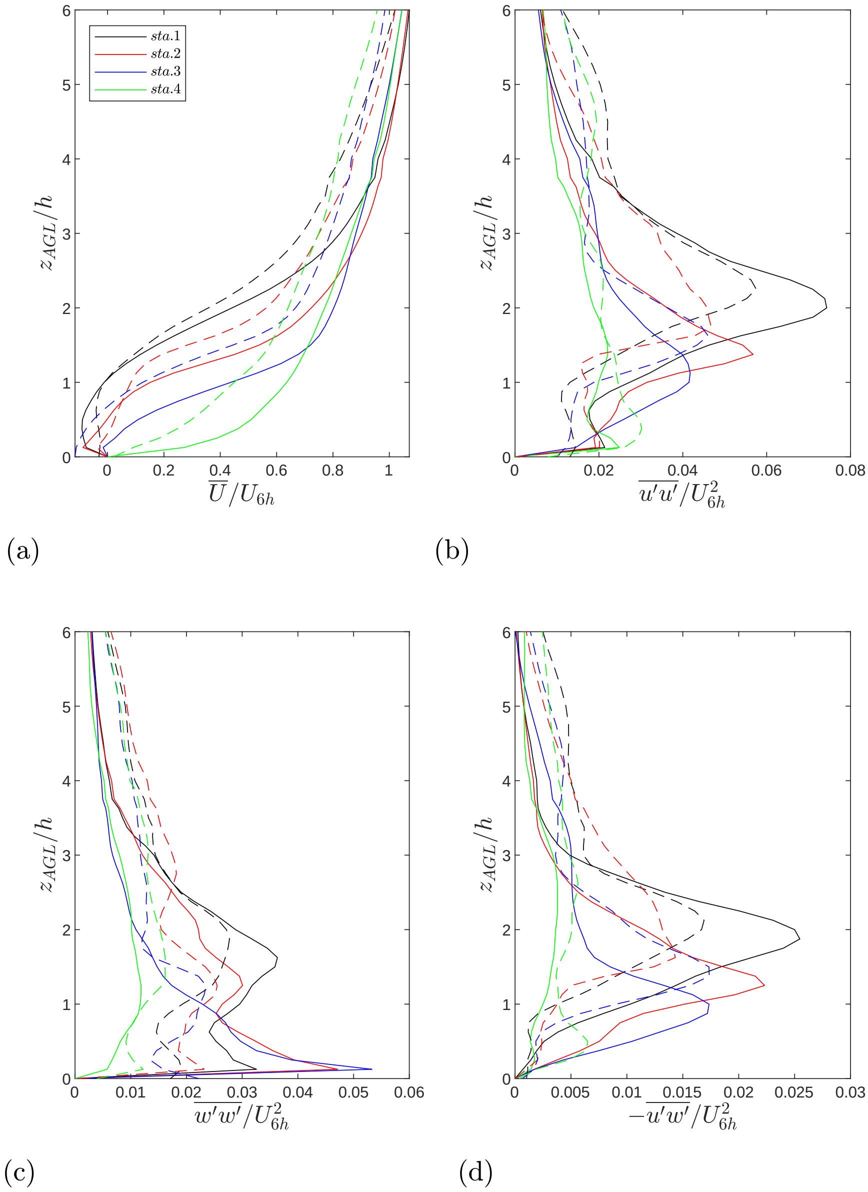

Fig. 14: Vertical profiles of a) streamwise mean velocity, b) streamwise normal stress, c) vertical normal stress and d)vertical Reynolds shear stress, at stations 1 − 4. Solid line, SF8 ext. Dashed line, ST8 ext. See the coordinates of the stations in Fig. 4

Figure 15 shows four mean streamwise velocity profiles at $y = -28$ m, -102 m, -152 m, and -210 m, at $z_{AGL} = 48$ m ($3h$) (see Fig. 4), of which the spanwise coordinates ($Y\ Loc.1$, $Y\ Loc.2$, $Y\ Loc.3$ and $Y\ Loc.4$) are respectively the same as the 4 stations ($sta.1$, $sta.2$, $sta.3$, and $sta.4$) in Fig. 14. Overall, the mean streamwise velocity profiles at the 4 spanwise locations over the flat terrain were highly similar in shape and magnitude with the corresponding ones over the real terrain, suggesting that the buildings played a dominant role, while the local terrain played a role of modulation. This was because the horizontal scale of the terrain elevation variation was much greater than building scale (see Figs. 2,4), albeit the terrain elevation magnitude was similar as the building height. For the $Y\ Loc.1$ profile there is a peak negative velocity at approximately $x = 700$ m, which is close to the tallest building in the campus. Within and immediate above the urban canopy, a positive correlation between the flat terrain and real terrain data was more complicated (Fig. 12a), but evident.

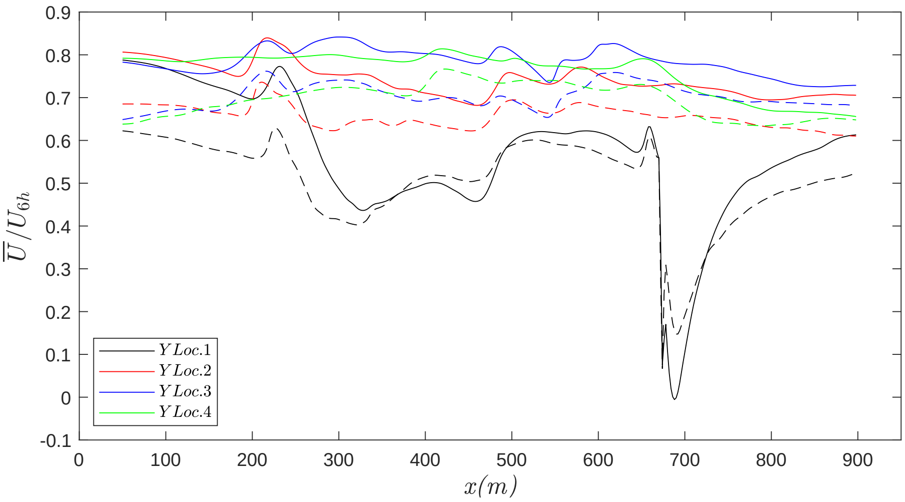

Fig. 15: Four streamwise mean velocity profiles along the streamwise direction, respectively at $y = -28$ m ($Y\ Loc.1$), -102 m ($Y\ Loc.2$), -152 m ($Y\ Loc.3$), and -210 m ($Y\ Loc.4$), and $z_{AGL} = 48$ m ($3h$) (Fig. 4). Solid line, SF8 ext. Dashed line, ST8 ext.

5.3 Internal Boundary Layers

The internal boundary layer (IBL) depth for both the flat (SF8 ext.) and real terrain (ST8 ext.) cases was estimated using the methodology proposed in Sessa et al. (2018) by determining the critical slope-change point of the spatially averaged vertical normal stress profiles $\overline{w'w'}$. The spatial average being calculated as defined below,

$$\langle \phi \rangle_s(x_m, z_{AGL}) = \frac{1}{2h \times Span} \int_{(x_m-h)}^{(x_m+h)} \left(\int_{(Span)} \phi(x, y, z_{AGL}) dy \right) dx, \quad (5)$$

where $\langle\rangle_s$ denotes the spatial average over a slice ($(x_m - h) \leq x \leq (x_m + h)$, -300 m $\leq y \leq 300$ m), which accounts for the span of the campus ($Span$). ϕ denotes the quantity (e.g. $\overline{w'w'}$) to be spatially-averaged. The comprehensive spatial average method of Xie and Fuka (2018) was used. This meant that where the average slice crossed a building all the solid regions at height z_{AGL} within the averaging region were included, but the value of the quantity was set to zero within them.

Figure 16 presents contour plots of the normalised spanwise averaged vertical normal stresses for cases SF8 ext. and ST8 ext, where the terrain surface was the lowest terrain elevation across the span. Overall, the two plots showed a similar developing internal boundary layer with an average thickness of about $4h$. At the centre of the domain ($x/h \approx 29$), the large $\overline{w'w'}$ value showed the north-south University Road crossed the entire campus. There were also some evident differences. At the west end of the campus, the internal boundary layer thickness over the real terrain increased abruptly due to local downslope starting from the west end of the campus up to the first valley. Immediately above the valley bottom surface, there was a region in which the values of $\overline{w'w'}$ were very low. This was because of the valley effect and the use of the comprehensive spatial average method(Eq. 5). Downwind of the University Road, the real terrain case ST8 ext. showed slower IBL spreading in the vertical direction, compared to the flat terrain case.

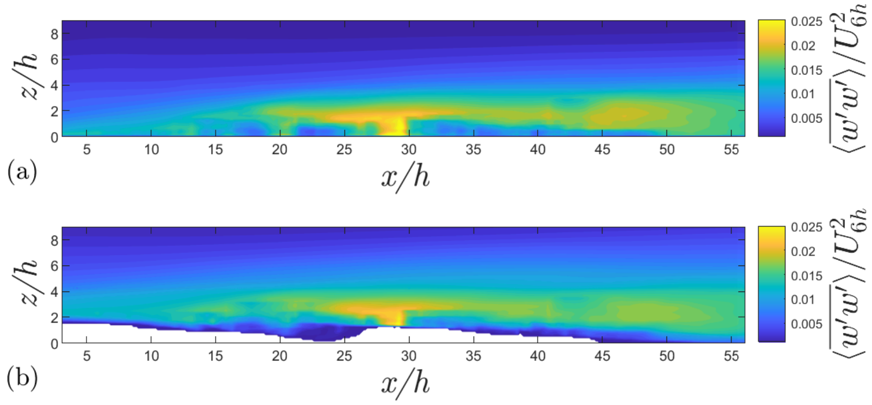

Fig. 16: Spanwise averaged normalised vertical normal stress for a) SF8 ext., and b) ST8 ext.

Figure 17a shows estimated IBL depths over the urban canopy for the flat (SF8 ext.) and real terrain (ST8 ext.) cases. To show an example of the estimation approach for the IBL depth, Figure 17b shows spanwise-averaged vertical normal stress $\overline{w'w'}$ for the flat terrain case at $(x - x_{LE})/h$=2, 6, 10, 14, 18, 22, 26 and 30, marked with the critical slope-change point (i.e. the intersection of the two straight lines). The critical slope-change in Fig. 17b was visible, but was not evident as that over a regular cuboid array in Sessa et al. (2018). This was because of the random nature of the array of buildings in the case SF8. ext, which generated a thicker but weaker shear layer above the canopy (e.g. Xie et al., 2008) than a uniform array. The average thickness above the ground level for SF8 ext. was about $4h$, whereas it was about $3h$ above ground level for a uniform array of cuboid blocks with a packing density 33% in Sessa et al. (2020). The random distribution of the building height, building size and spacing in the case SF8 ext. were the main factors causing the fast growth of the IBL thickness.

The interface of the internal and external boundary layers over the real terrain was much more difficult to identify than that over the flat terrain. Considering the uncertainties due to the variation of terrain elevation in the near-inlet region, only the IBL thickness downstream of $x = 10h + x_{LE}$ was estimated. The IBL thickness for case ST8 ext. measured from $z = 0$ was close to that for case SF8 ext. while measured from the local ground level it was slightly less than that for case SF8 ext. Figure 17a shows that the IBL thickness curves for both cases oscillated while the IBL progressed downstream, differing from that over a uniform array of buildings (e.g. Sessa et al., 2018). The oscillations were caused by changes in the elevation of the underlying surface, i.e. buildings and terrain.

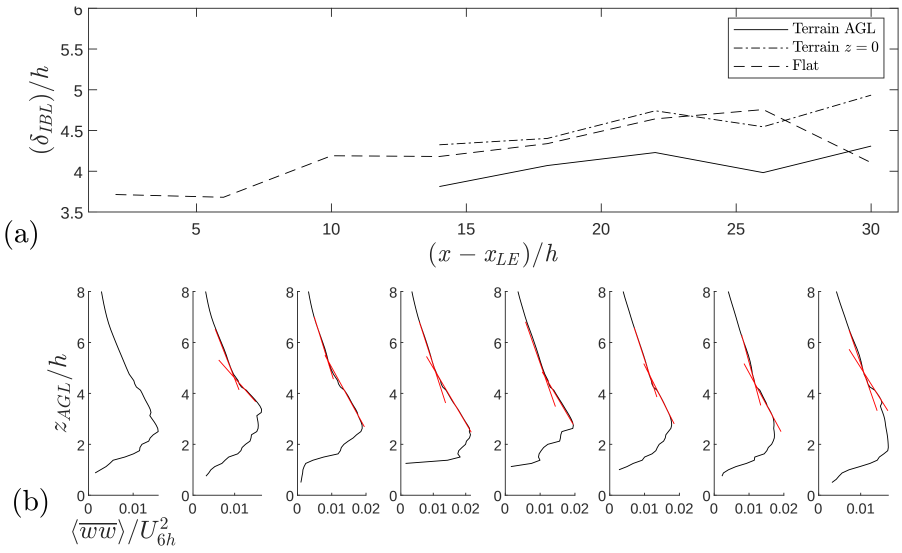

Fig. 17: a) Development of IBL (AGL) from the leading edge of the canopy, for flat (SF8 ext.) and real (ST8 ext.) terrain cases. The leading edge of the canopy occurs at $x_{LE} = 14h$ in Fig. 17. b) Spanwise-averaged vertical normal stress $\overline{w'w'}$ over the flat terrain (SF8 ext.), marked with the critical slope-change point (i.e. the intersection of the two straight lines)

6 Concluding Remarks and Discussion

LES simulations were carried out to simulate atmospheric airflows over the University of Southampton Highfield Campus considering both flat and real terrains, with the aim of quantifying and understanding the impact of street scale (O(0.1 km)) variations in urban terrain on urban aerodynamics and turbulent boundary layer quantities. It is to be noted that the current case study is a considerably simplified one for terrain effect. Further studies should consider thermal stratification, tree effect and various wind directions.

To assess the sensitivity of the results to uncertainties in the inflow turbulence quantities input to the synthetic turbulence inflow conditions, simulations were made with data from two experimental sources. The first was “simulated atmospheric boundary layer” data generated from the University of Surrey EnFlo wind tunnel, the second was naturally generated boundary layer data from the water tunnel at the University of Southampton. The LES data showed that turbulence statistics sampled at a sufficiently large distance from the inlet (e.g. more than 10 average building heights), within and immediately above the urban canopy, were relatively insensitive to the precise inflow Reynolds stresses, given the same inflow integral length scale and mean streamwise velocity. This does not undermine the idea that street and city scales of airflow are coupled as there were substantial differences in the turbulence quantities above twice average building height.

A systematic comparison of LES predictions of atmospheric airflows over the flat and real terrains showed that capturing terrain effects was crucial, where the height variation of a street-scale (O(0.1 km) topographic feature was of the same order of magnitude as the neighbourhood buildings. This was perhaps what one would expected. The ratio between realistic and flat terrains of time-mean streamwise velocity at the same ground level height over a terrain crest location can be greater than 2, while over a valley trough it can be less than 0.5. The correlation between the mean streamwise velocity and the terrain elevation is evident within and immediately above the urban canopy, despite the disturbance due to the buildings. To enable corrections to be developed for experimental and numerical data acquired from flat terrain simulations, it is crucial to quantify and understand how street-scale terrain variations modulate the local mean velocity and turbulence statistics at a given above-ground level (AGL) height.

The global (average) gradient of the west-east downslope of the studied domain is much smaller ($\approx 2.3^\circ$) than the local terrain gradients, and contributes little to the evident modulations observed in the local mean velocity field. The small global gradient yields negligible discrepancy in the horizontally averaged mean streamwise velocity against the AGL height.

The significant impact from the local terrain features (O(0.1 km)) on the local airflow and turbulence, and on the global quantities, such as the depth of the spanwise-averaged internal boundary layer and spatially-averaged turbulent kinetic energy (TKE), highlights the crucial importance of taking it into account of the prognostic numerical models. In the micro-scale engineering type models, a fine mesh for resolving these small terrain feature, as well as the buildings, is an option for improving the prediction of near-field dispersion and the urban micro-climate. Such small terrain features in a grid of the future high-resolution meso-scale models of a mesh resolution (O(0.1 km)) is considered as a heterogeneous underlying surface, and an advanced parameterisation for an inclusion of the heterogeneity effect is required.

Acknowledgements

MC is grateful to the Faculty of Engineering and the Environments for providing the PhD studentship. MC and ZTX thank Drs Tim Foat and Davide Lasagna for providing insight and support. ZTX and MC are also grateful to the UK Natural Environment Research Council for providing financial support (NE/W002841/1) to the further data analysis and writing of the paper. The authors are grateful to the three anonymous reviewers for their valuable comments. Computational work was undertaken on the University of Southampton Iridis systems, and experimental work in the University of Southampton water tunnel.

Declarations

Ethical Approval

Not applicable.

Competing interests

No, I declare that the authors have no competing interests as defined by Springer, or other interests that might be perceived to influence the results and/or discussion reported in this paper.

Authors' contributions

Coburn: carried out simulations, experiments and analysis; prepared figures, wrote the main manuscript text. Vanderwel: supervised the experimental work; prepared the experimental facilities. Herring: supervised the design of the study, reviewed and edited the MS. Xie: Project administration; supervised simulations and analysis; wrote the main manuscript text. All authors reviewed the manuscript.

Funding

1. Natural Environment Research Council, NE/W002841/1.
2. the Faculty of Engineering and the Environments, PhD studentship.

Availability of data and materials

The datasets generated during and/or analysed during the current study are available from the corresponding author on reasonable request.

Conflict of interest

The authors declare that they have no conflict of interest.

References

Antoniou N, Montazeri H, Wigo H, Neophytou MKA, Blocken B, Sandberg M (2017) CFD and wind-tunnel analysis of outdoor ventilation in a real compact heterogeneous urban area: Evaluation using "air delay". Building and Environment 126:355–372

Apsley DD, Castro IP (1997) Flow and dispersion over hills: comparison between numerical predictions and experimental data. Journal of Wind Engineering and Industrial Aerodynamics 67:375–386

Arnold S, ApSimon H, Barlow J, Belcher S, Bell M, Boddy J, Britter R, Cheng H, Clark R, Colvile R, et al. (2004) Introduction to the DAPPLE air pollution project. Science of the Total Environment 332(1-3):139–153

Barlow J, Best M, Bohnenstengel SI, Clark P, Grimmond S, Lean H, Christen A, Emeis S, Haeffelin M, Harman IN, et al. (2017) Developing a research strategy to better understand, observe, and simulate urban atmospheric processes at kilometer to subkilometer scales. Bulletin of the American Meteorological Society 98(10):ES261–ES264

Blocken B, van der Hout A, Dekker J, Weiler O (2015) CFD simulation of wind flow over natural complex terrain: Case study with validation by field measurements for ria de ferrol, galicia, spain. Journal of Wind Engineering and Industrial Aerodynamics 147:43–57

Castro IP, Xie ZT, Fuka V, Robins AG, Carpentieri M, Hayden P, Hertwig D, Coceal O (2017) Measurements and computations of flow in an urban street system. Boundary-Layer Meteorology 162(2):207–230

Cheng H, Castro IP (2002) Near wall flow over urban-like roughness. Boundary-Layer Meteorology 104(2):229–259

Coburn M, Xie ZT, Herring SJ (2022) Numerical simulations of boundary-layer airflow over pitched-roof buildings. Boundary-Layer Meteorology 185(3):415–442

Conan B, Chaudhari A, Aubrun S, van Beeck J, Hämäläinen J, Hellsten A (2016) Experimental and numerical modelling of flow over complex terrain: the bolund hill. Boundary-layer meteorology 158(2):183–208

Counihan J (1969) An improved method of simulating an atmospheric boundary layer in a wind tunnel. Atmospheric Environment (1967) 3(2):197–214

Fernando HJS (2010) Urban atmospheres in complex terrain. Annu Rev Fluid Mech 42:365–89

Fossum HE, Helgeland A (2020) Computational fluid dynamics simulations of local wind in large urban areas (20/02365). In: Tech. rep., Norwegian Defence Research Establishment (FFI)

Fuka V, Xie ZT, Castro IP, Hayden P, Carpentieri M, Robins AG (2018) Scalar fluxes near a tall building in an aligned array of rectangular buildings. Boundary-layer meteorology 167(1):53–76

Goulart EV, Reis Jr N, Lavor VF, Castro IP, Santos JM, Xie ZT (2019) Local and non-local effects of building arrangements on pollutant fluxes within the urban canopy. Building and Environment 147:23–34

Gronemeier T, Surm K, Harms F, Leitl B, Maronga B, Raasch S (2020) Validation of the dynamic core of the palm model system 6.0 in urban environments: LES and wind-tunnel experiments. Geoscientific Model Development Discussions pp 1–26

Han BS, Park SB, Baik JJ, Park J, Kwak KH (2017) Large-eddy simulation of vortex streets and pollutant dispersion behind high-rise buildings. Quarterly Journal of the Royal Meteorological Society 143(708):2714–2726

Hanna S, Tehranian S, Carissimo B, Macdonald R, Lohner R (2002) Comparisons of model simulations with observations of mean flow and turbulence within simple obstacle arrays. Atmospheric Environment 36(32):5067–5079
Hertwig D, Efthimiou GC, Bartzis JG, Leitl B (2012) CFD-RANS model validation of turbulent flow in a semi-idealized urban canopy. Journal of Wind Engineering and Industrial Aerodynamics 111:61–72
Hertwig D, Gough HL, Grimmond S, Barlow JF, Kent CW, Lin WE, Robins AG, Hayden P (2019) Wake characteristics of tall buildings in a realistic urban canopy. Boundary-Layer Meteorology 172(2):239–270
Inagaki A, Kanda M, Ahmad NH, Yagi A, Onodera N, Aoki T (2017) A numerical study of turbulence statistics and the structure of a spatially-developing boundary layer over a realistic urban geometry. Boundary-Layer Meteorology 164(2):161–181
Inagaki M, Kondoh T, Nagano Y (2005) A mixed-time-scale SGS model with fixed model-parameters for practical les. J Fluids Eng 127(1):1–13
Kanda M, Moriwaki R, Kasamatsu F (2004) Large-eddy simulation of turbulent organized structures within and above explicitly resolved cube arrays. Boundary-Layer Meteorology 112(2):343–368
Lim H, Hertwig D, Grylls T, Gough H, Reeuwijk Mv, Grimmond S, Vanderwel C (2022) Pollutant dispersion by tall buildings: laboratory experiments and large-eddy simulation. Experiments in Fluids 63(6):92
Limbrey EG, Macdonald JH, Rees J, Xie ZT (2016) Modelling the airflow at the clifton suspension bridge site. In: 12th UK Conference on Wind Engineering,Nottingham, The UK Wind Engineering Society
Liu Y, Liu CH, Brasseur GP, Chao CY (2023) Wavelet analysis of the atmospheric flows over real urban morphology. Science of the Total Environment 859:160,209
Macdonald R, Carter S, Slawson PR (2000) Measurements of mean velocity and turbulence statistics in simple obstacle arrays at 1: 200 scale. Thermal Fluids Report 1
Ricci A, Kalkman I, Blocken B, Burlando M, Repetto M (2020) Impact of turbulence models and roughness height in 3d steady RANS simulations of wind flow in an urban environment. Building and Environment 171:106,617
Sessa V, Xie ZT, Herring S (2018) Turbulence and dispersion below and above the interface of the internal and the external boundary layers. Journal of Wind Engineering and Industrial Aerodynamics 182:189–201
Sessa V, Xie ZT, Herring S (2020) Thermal stratification effects on turbulence and dispersion in internal and external boundary layers. Boundary-Layer Meteorology 176(1):61–83
Stoesser T, Mathey F, Frohlich J, Rodi W (2003) Les of flow over multiple cubes. Ercoftac Bulletin 56:15–19
Tolias I, Koutsourakis N, Hertwig D, Efthimiou G, Venetsanos A, Bartzis J (2018) Large eddy simulation study on the structure of turbulent flow in a complex city. Journal of Wind Engineering and Industrial Aerodynamics 177:101–116

Wingstedt EMM, Osnes AN, Åkervik E, Eriksson D, Reif BP (2017) Large-eddy simulation of dense gas dispersion over a simplified urban area. Atmospheric Environment 152:605–616

Xie ZT, Castro IP (2006) LES and RANS for turbulent flow over arrays of wall-mounted obstacles. Flow, Turbulence and Combustion 76(3):291

Xie ZT, Castro IP (2008) Efficient generation of inflow conditions for large eddy simulation of street-scale flows. Flow, turbulence and combustion 81(3):449–470

Xie ZT, Castro IP (2009) Large-eddy simulation for flow and dispersion in urban streets. Atmospheric Environment 43(13):2174–2185

Xie ZT, Fuka V (2018) A note on spatial averaging and shear stresses within urban canopies. Boundary-layer meteorology 167(1):171–179

Xie ZT, Coceal O, Castro IP (2008) Large-eddy simulation of flows over random urban-like obstacles. Boundary-layer meteorology 129:1–23